

DESORPTION KINETICS AND BINDING ENERGIES OF SMALL HYDROCARBONS

AIDA BEHMARD¹

¹Division of Geological and Planetary Sciences, California Institute of Technology, Pasadena, CA 91125, USA

EDITH C. FAYOLLE^{2,3}, DAWN M. GRANINGER⁴, JENNIFER B. BERGNER², RAFAEL MARTÍN-DOMÉNECH², PAVLO MAKSYUTENKO²,
MAHESH RAJAPPAN², AND KARIN I. ÖBERG²

²Harvard-Smithsonian Center for Astrophysics, 60 Garden Street, Cambridge, MA 02138, USA

³Jet Propulsion Laboratory, California Institute of Technology, 4800 Oak Grove Drive, Pasadena, CA 91109-8099, USA and

⁴Lawrence Livermore National Laboratory, 7000 East Avenue, Livermore, CA 94550, USA

(Received: Accepted)

Draft version March 26, 2019

ABSTRACT

Small hydrocarbons are an important organic reservoir in protostellar and protoplanetary environments. Constraints on desorption temperatures and binding energies of such hydrocarbons are needed for accurate predictions of where these molecules exist in the ice vs. gas-phase during the different stages of star and planet formation. Through a series of temperature programmed desorption (TPD) experiments, we constrain the binding energies of 2 and 3-carbon hydrocarbons (C₂H₂ - acetylene, C₂H₄ - ethylene, C₂H₆ - ethane, C₃H₄ - propyne, C₃H₆ - propene, and C₃H₈ - propane) to 2200–4200 K in the case of pure amorphous ices, to 2400–4400 K on compact amorphous H₂O, and to 2800–4700 K on porous amorphous H₂O. The 3-carbon hydrocarbon binding energies are always larger than the 2-carbon hydrocarbon binding energies. Within the 2- and 3-carbon hydrocarbon families, the alkynes (i.e., least-saturated) hydrocarbons exhibit the largest binding energies, while the alkane and alkene binding energies are comparable. Binding energies are ~5–20% higher on water ice substrates compared to pure ices, which is a small increase compared to what has been measured for other volatile molecules such as CO and N₂. Thus in the case of hydrocarbons, H₂O has a less pronounced effect on sublimation front locations (i.e., snowlines) in protoplanetary disks.

Keywords: laboratory: molecular — protoplanetary disks — astrochemistry

1. INTRODUCTION

Simple hydrocarbons are common in protostellar and circumstellar environments (Tucker et al. 1974; Betz 1981; Öberg et al. 2008; Pontoppidan et al. 2014; Guzmán et al. 2015), and may constitute an important reservoir of volatile carbon during planet formation. In Solar System comets, which are thought to preserve the volatile composition of the outer Solar Nebula, hydrocarbon detections include CH₄, C₂H₂, and C₂H₆ (Mumma et al. 1996; Brooke et al. 1996; Hudson & Moore 1997; Kawakita et al. 2014). Hydrocarbons have also been detected in Solar Nebula analogs: C₂H and *c*-C₃H₂ at millimeter / sub-millimeter wavelengths, CH₄ in the near-IR, C₂H₂ in the mid and near-IR, and the hydrocarbon radical CH⁺ in the far-IR (Lahuis et al. 2006; Gibb et al. 2007; Thi et al. 2011; Qi et al. 2013; Gibb & Horne 2013; Pontoppidan et al. 2014; Kastner et al. 2015). Larger hydrocarbons, such as C₃H₄ and C₃H₆, are expected to be present in disks and comets since they are frequently observed during early stages of star formation (Markwick et al. 2002), but have yet to be detected (Snyder & Buhl 1973).

In interstellar and circumstellar environments, hydrocarbons can form through several pathways. During the early stages of cloud formation, when the majority of carbon in the gas phase is in the form of atomic carbon, unsaturated hydrocarbons form efficiently through ion-molecule gas-phase chemistry (e.g., Agúndez & Wakelam 2013). These carbon atoms can also adsorb onto grain surfaces where hydrogen addition to adsorbed atomic carbon leads to the formation of CH₄ (e.g., Tielens & Hagen 1982). CH₄ and other small hydrocarbons can then serve as starting points for larger hy-

drocarbon formation, both through grain surface reactions (Moore & Hudson 1998; Öberg et al. 2010), and through gas-phase reactions following desorption (Charnley 2004; Sakai & Yamamoto 2013). Warm carbon chain chemistry (WCCC) is initiated by CH₄ sublimation from icy grain mantles and leads to the formation of long, unsaturated carbon chains (Sakai & Yamamoto 2013; Graninger et al. 2016). In the solid state, hydrocarbon-rich ices are proposed to be the starting point of a rich prebiotic chemistry (Kaiser & Roessler 1998; Bernstein et al. 2005; Hardegree-Ullman et al. 2014). Gas-phase reactions are proposed as a major source of hydrocarbons in the envelopes of protostars (Sakai & Yamamoto 2013; Graninger et al. 2016).

Hydrocarbons formed during the pre- and protostellar stages of star formation are likely inherited by the protoplanetary disk. In the disk, hydrocarbon chemistry may proceed to produce a new, distinct set of products, though the relative importance of inheritance and in situ chemistry for organic molecules is still debated (e.g., Cleaves et al. 2016). In either case, predicting how hydrocarbons are incorporated into planetesimals and planetary atmospheres requires understanding their division between gas and ice phases throughout protoplanetary disks. This division is set by the locations of hydrocarbon sublimation fronts, and by the ease with which hydrocarbons are entrapped in less volatile ices. Both are important to quantify. This study addresses the former process.

The sublimation front locations of molecular species are dictated by adsorption and desorption kinetics, which are in turn set by their binding energies (e.g., Viti et al. 2004; Hollenbach et al. 2009; He et al. 2016, 2017). Some constraints on binding energies exist for CH₄, C₂H₂, C₂H₆, and C₃H₈

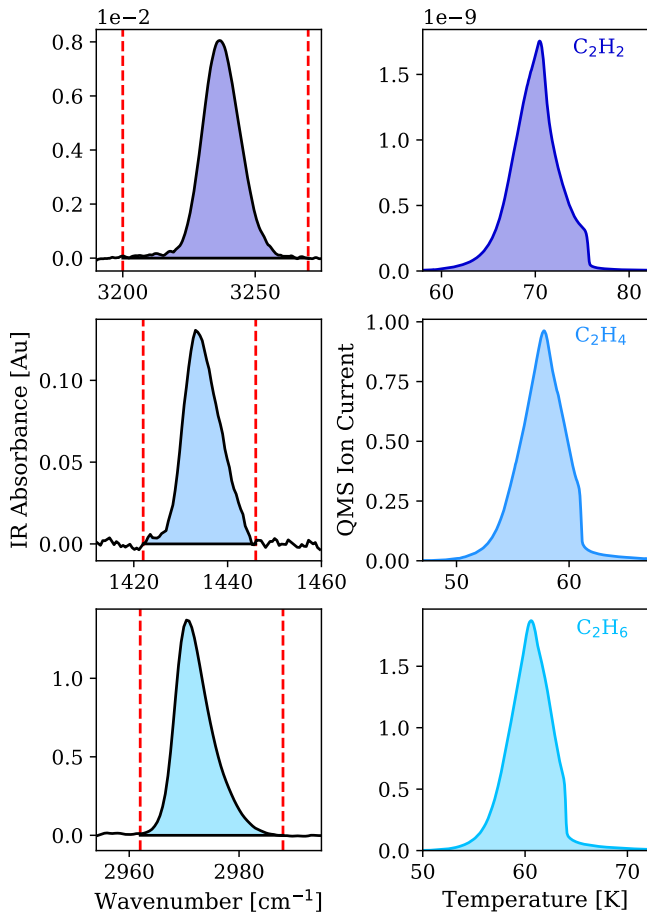


Figure 1. The left column displays the strongest IR features that were used to estimate the ice thicknesses for each pure C_2H_x TPD, with the shaded regions identifying the integrated regions. The right column displays the pure 2-carbon TPDs that were used as references to estimate the thicknesses of C_2H_x TPDs on compact water substrates.

from different experimental studies (Collings et al. 2004; He et al. 2016; Smith et al. 2016). We expand on these through a survey of desorption behavior for all linear 2-3 carbon hydrocarbons. Both pure ice desorption and desorption off H_2O substrates are investigated. Among these experiments, desorption off compact H_2O ice is the most relevant for the majority of astrophysical environments (Boogert et al. 2015). In Section 2 we present the experimental setup and methods used to characterize hydrocarbon desorption. The experimental results and the binding energies are presented in Section 3 and discussed in Section 4, and some astrophysical implications are presented in Section 5.

2. METHODS

2.1. Experimental Details

TPD experiments were conducted in an ultra-high vacuum (UHV) chamber described in detail by Lauck et al. (2015). The UHV chamber has a base pressure of $<5 \times 10^{-10}$ Torr at room temperature, dominated by H_2 . Amorphous ices were grown on a 0.75 inch diameter and 2 mm thick CsI window at the center of the chamber that can be cooled to 11 K by a closed-cycle He cryostat. Unless otherwise noted, all ices used in TPD experiments throughout this study are amorphous in structure, which is most relevant for interstellar environments (Hagen et al. 1981; Oba et al. 2009).

Gaseous C_2H_2 - acetylene (99.6% Matheson Trigas)¹ C_2H_4 - ethylene (99.99% Sigma-Aldrich), C_2H_6 - ethane (99.99% Sigma-Aldrich), C_3H_4 - propyne ($\geq 99\%$ Sigma-Aldrich), C_3H_6 - propene ($\geq 99\%$ Sigma-Aldrich), and C_3H_8 - propane (99.97% Sigma-Aldrich) were deposited through a 4.8 mm diameter pipe with the outlet located 0.8 inches from the CsI window onto the bare 11 K CsI window or onto thick amorphous compact / porous H_2O ice substrates. The H_2O was purified beforehand through at least three freeze-pump-thaw cycles using liquid nitrogen. H_2O substrates were grown by depositing deionized H_2O at 100 K for compact substrates, followed by cool-down to 11 K, and at 11 K for porous substrates. Deposition temperature influences ice structure (compact v. porous) due to molecular rearrangement resulting from thermal diffusion (e.g., Bossa et al. 2012; Clements et al. 2018). The degree of porosity can be determined from the intensity of the dangling O-H bond spectral feature (Devlin & Buch 1995). However, we were unable to investigate the porosity of our water films via the dangling O-H bond as it is not well detected in our ices (see Fig. A.1, left panel; the dangling O-H bond would be visible at $\sim 3600\text{--}3700\text{ cm}^{-1}$). This indicates that the porosity of our porous water films is low, but does not indicate a total lack of porosity (Raut et al. 2007; Isokoski et al. 2014). Laboratory studies also show that the dangling O-H bond cannot be used to investigate porosity quantitatively (e.g., Bossa et al. 2014). To investigate this further, we conducted additional TPD experiments of CO on compact and porous H_2O substrates, and found that the TPD curve of the porous experiment exhibits a CO desorption peak around the H_2O desorption temperature, while that of the compact experiment does not (see Fig. A.1, right panel). This provides additional evidence that our porous substrates do indeed contain pores. We confirmed that the H_2O ices were amorphous rather than crystalline in structure from the shapes of the H_2O IR spectral bands (e.g., Mastrapa et al. 2009).

Following deposition, infrared spectra of ice films were taken using a Fourier transform infrared spectrometer (FTIR, Bruker Vertex 70v) in transmission mode. To produce a single spectrum, 128 scans were averaged over the $4000\text{--}600\text{ cm}^{-1}$ spectrometer range at a resolution of 1 cm^{-1} . TPD measurements were performed by linearly heating the prepared ices at 2 K min^{-1} and monitoring the desorbing molecules using a quadrupole mass spectrometer (QMS, Pfeiffer QMG 220M1) until complete hydrocarbon desorption. The CsI window temperature was monitored and increased using a temperature controller (LakeShore 355) that operates a heating element situated above the window holder and silicon diode sensors attached onto the window holder. The measured temperature has an estimated accuracy of 2 K and a relative uncertainty of 0.1 K. We obtained TPD plots in desorbing molecules K^{-1} by scaling the main hydrocarbon fragment ion current from the QMS using factors derived from methods explained in Section 2.2.

2.2. Ice Thicknesses

This study presents data on pure hydrocarbon ice desorption, and hydrocarbon desorption off compact and porous

¹ The C_2H_2 was dissolved in acetone, accounting for its relatively low purity. One should note that we used C_2H_2 straight from the bottle without any purification steps because no acetone was detected by quadrupole mass spectrometer analysis during deposition, and no acetone IR features were observed in the FTIR spectrum of deposited C_2H_2 .

H₂O ice. Pure hydrocarbon desorption requires ice thicknesses greater than a few monolayers to ensure that the initial desorption curve is dominated by hydrocarbon-hydrocarbon interactions. In the cases of desorption off H₂O substrates, ice thicknesses should be in the mono- or submonolayer regime where the kinetics are dominated by hydrocarbon-H₂O interactions. Ice thickness measurements are required to first ensure that the experiments are carried out in the correct desorption regime, and later to extract binding energies from TPD curves. We also use the estimated ice thicknesses for each experiment to convert the QMS ion current to a desorption rate in units of molecules K⁻¹.

We used three different methods to determine hydrocarbon ice thicknesses: IR spectroscopy (for the pure C₂H_x ices), integrated ion currents from the TPD experiments (for the pure C₃H_x ices and all hydrocarbons desorbing off compact water), and TPD shape characteristics (for all hydrocarbons desorbing off porous water). Errors on ice thicknesses determined from any method other than IR band strengths are taken as 50%. The ice thicknesses are given in monolayer units with the typical approximation of 1 ML = 10¹⁵ molecules cm⁻². However, 1 ML does not always correspond to one molecular layer; porous surfaces are rougher than compact surfaces, allowing them to accommodate more molecules upon a surface area unit. At the same time, porous surfaces contain pores that can trap molecules and inhibit their release via desorption. By comparing thicknesses calculated from IR bands strengths versus using porous experiments as thickness calibrations, we found that these effects roughly cancel each other out, and that the porous H₂O TPDs provide a reasonable measure of the ion current corresponding to 1 ML.

To determine pure C₂H_x ice thicknesses with IR spectroscopy, we used post-deposition IR spectra and hydrocarbon band strengths. Band strengths relevant for the C₂H_x hydrocarbons in our set are reported in Hudson et al. (2014a), Hudson et al. (2014b), and Gerakines et al. (1995) (Fig. 1, left panel). All IR modes and associated band strengths used in this work are reported in Table 1. Thicknesses were calculated from the formula:

$$N_i = \frac{\ln(10) \int I(\nu) d\nu}{A_i} \quad (1)$$

where N_i is the column density (molecule cm⁻²), $\int I(\nu) d\nu$ is the integrated area of the IR band (absorbance units), and A_i is the band strength in optical depth units as reported in the literature. Though reported band strength errors are between 0.5–6%, we adopted an error of 20% on all band strengths to account for possible differences in temperature and ice structure between our study and those from which the band strengths were extracted. A 20% error is also consistent with the variance in ice thickness measurements we obtain when different IR bands are chosen for the calculation.

Pure C₃H_x ice thicknesses could not be measured with IR spectroscopy due to the lack of C₃H_x band strengths reported in the literature. Instead, they are estimated from their integrated TPD curves using the C₃H_x porous experiments as references, which are assumed to have thicknesses of ~1 ML (justified below). In any case, to ensure that the pure ice experiments (both 2- and 3-carbon) were in the multilayer regime where energies are independent of thickness, we ran a series of TPD experiments of increasing thickness and checked for overlapping leading edges (Fig. 2).

We estimated the thicknesses of ices (both 2- and 3-carbon

Table 1
IR Band Positions and Strengths

Molecule	IR Mode	Position (cm ⁻¹)	Band Strength A_i (cm molecule ⁻¹)
H ₂ O	ν_1	3280	2.0×10^{-16}
C ₂ H ₂	ν_5	3240	2.39×10^{-17}
C ₂ H ₄	ν_7	1434.3	2.24×10^{-18}
C ₂ H ₆	ν_5	2972.3	2.20×10^{-17}

Note: Errors on all band strengths are uniformly set at 20%. For justification, see Section 2.2.

hydrocarbons) on porous H₂O by noting that the TPD curves of all experiments involving porous substrates deviate from the profile expected for pure submonolayer coverages by exhibiting a small multilayer peak, indicating that they are on the verge of reaching the multilayer desorption regime and thus correspond to ~1 ML coverage (Fig. 3).

For experiments of hydrocarbon desorption off compact H₂O, we aimed to deposit submonolayer coverages of hydrocarbon ice onto a ~50 ML H₂O ice substrate. The hydrocarbon ice thicknesses could not be verified with IR spectroscopy because IR bands of thin ices are weak and broad in the presence of H₂O. To obtain ice thicknesses for C₂H_x ices on compact substrates, we compared the integrated areas of their TPD curves (ion current in A · s) to those of the pure ice experiments, and multiplied the integrated TPD ratios with the known ice thicknesses of the pure experiments. (Fig. 1, right panel) (e.g., Doronin et al. 2015; Bertin et al. 2011). This method assumes that the QMS signal is proportional to the number of desorbing molecules and that the chamber vacuum pump is evacuating gas at a high speed, both of which have been experimentally verified. Because the C₃H_x band strengths are unknown, we could not use this procedure to estimate the thicknesses of 3-carbon ices on compact substrates. Instead, we used the integrated ion current ratios with the 3-carbon ices on porous substrates as references, as in the case of determining the pure 3-carbon ice thicknesses.

We chose compact ice experiments with coverages of ~0.2 ML to ensure that we were in the regime where hydrocarbon-H₂O interactions dominate. Ideally, we wanted the thinnest coverages possible to isolate these interactions, but found that desorption of films thinner than ~0.2 ML did not produce detectable signals in the TPD data. Our choice of ~0.2 ML coverages on compact substrates is further discussed in Section 3.2.

2.3. Modeling

To obtain binding energies, we fit the TPD curves with the Polanyi-Wigner equation:

$$-\frac{d\theta}{dT} = \frac{\nu}{\beta} \theta^n e^{-E_b/T} \quad (2)$$

where n is the desorption order, θ is the ice coverage, T is the temperature in K, ν is a pre-exponential factor in ML^(1- n) s⁻¹, β is the heating rate in K s⁻¹, and E_b is the binding energy in K.

For pure ices, we determined the hydrocarbon binding energies by fitting the TPD curves using zeroth-order kinetics ($n = 0$ in Equation 1). We calculated E_b and the pre-exponential factor ν simultaneously by fitting the logarithm of the desorp-

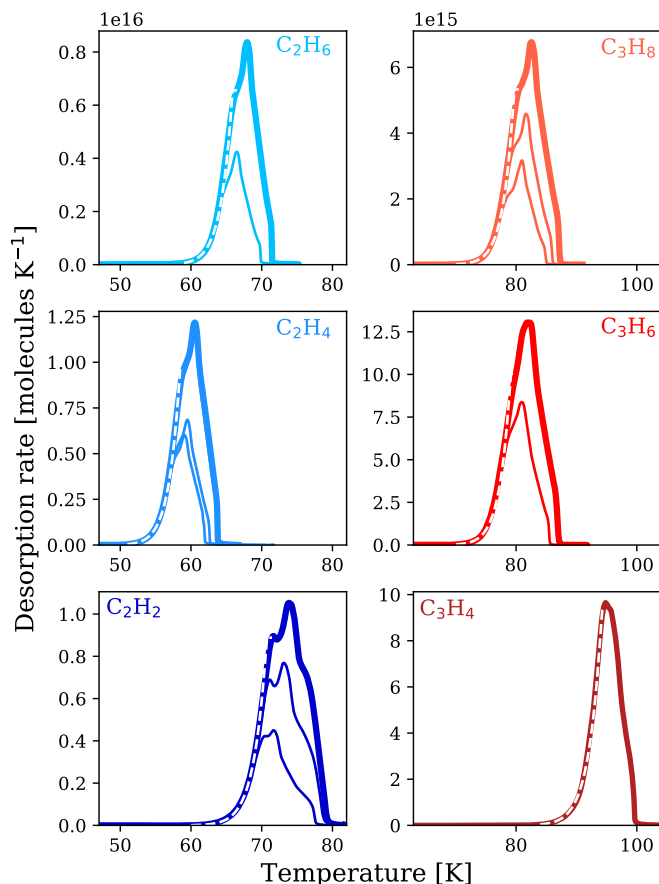


Figure 2. Pure 2-carbon (left) and 3-carbon (right) hydrocarbon TPD curves displayed in solid colored lines, with overlaid white dashed lines representing the fit to obtain the binding energies. When available, TPD runs of thinner ices are overlaid in thinner solid colored lines to demonstrate that the zeroth-order regime was achieved. In the case of C_3H_4 , the first TPD curve we acquired clearly showed zeroth order kinetics and we therefore did not gather additional, supporting data.

tion rate versus the inverse of the temperature with a straight line. The process is illustrated in Fig. A.2.

The hydrocarbon- H_2O TPDs are fitted with the first-order ($n = 1$ in Equation 1) form of the Polanyi-Wigner equation as is appropriate for submonolayer desorption where the ice system is characterized by a single binding energy. The non-homogeneous nature of amorphous water ice results in surfaces with a range of binding sites. We therefore fit the submonolayer interaction of the curve with a distribution of binding energies described by a linear combination of first-order desorption kinetics (Noble et al. 2012; Collings et al. 2015; Doronin et al. 2015; Fayolle et al. 2016). This is accomplished by sampling a range of binding energies in steps of 60–100 K. We used a range of 1800–3700 K for 2-carbon hydrocarbons and 3900–5500 K for 3-carbon hydrocarbons on compact substrates, and a range of 2700–5000 K for 2-carbon hydrocarbons and 3000–5500 K for 3-carbon hydrocarbons on porous substrates. An alternative method for modeling submonolayer desorption is presented in Smith et al. (2016), which differs from our approach by modeling the binding energy as a continuous function of coverage. However, we note that our chosen step sizes are well within the binding energy errors and should thus not be a major contributor to the binding energy distribution uncertainties.

We obtain a binding energy distribution from which a mean

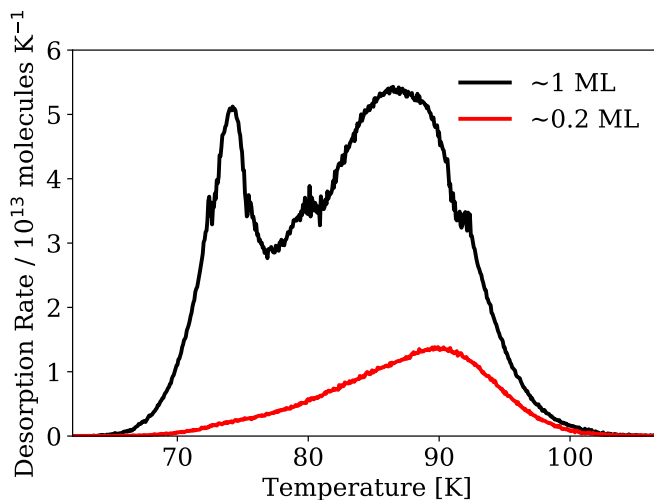


Figure 3. TPD curves of two different C_3H_6 coverages on porous H_2O substrates. The loss of the multilayer peak from the first to the second TPD marks the transition from the multilayer to the submonolayer regime.

E_b and associated FWHM can be extracted assuming a Gaussian distribution. Pre-exponential factors ν derived from the multilayer regime calculations are used in the monolayer and submonolayer regime calculations. For more details on the binding energy calculation procedures, see Fayolle et al. (2016). Errors on calculations take into account the estimated accuracy of 2 K and relative uncertainty of 0.1 K on the temperature instrument as well as errors on ice thickness (see Section 3.2).

3. RESULTS

3.1. Temperature Programmed Desorption Curves

A summary of all experiments is provided in Table 2. TPD curves on CsI, compact H_2O , and porous H_2O substrates are displayed in Fig. 4.

Pure Hydrocarbon Ices – On CsI substrates, 2-carbon hydrocarbons all exhibit lower desorption temperatures than 3-carbon hydrocarbons. Within the 2-carbon hydrocarbon set, C_2H_4 exhibits the lowest desorption temperature, followed by C_2H_6 and lastly C_2H_2 . The same desorption temperature trend of alkene, alkane, alkyne is exhibited within the 3-carbon hydrocarbon set, with C_3H_6 exhibiting the lowest desorption temperature, followed by C_3H_8 and C_3H_4 (Fig. 2).

The TPD curves of 2-carbon hydrocarbons and C_3H_8 exhibit fall off from the initial leading edge, resulting in "bump"-like features (Fig. 4). These "bumps" may be due to an amorphous-to-crystalline transition. There are studies that have constrained the temperatures at which amorphous-to-crystalline transitions are expected to occur for 2-carbon hydrocarbons (e.g., Anderson et al. 1985; Khanna et al. 1988; Zhao et al. 1988; Hudson et al. 2014a,b), and these are generally consistent with the temperature points of the "bumps" in our pure 2-carbon TPD curves (Fig. 2). Whether the bumps observed in the 3-carbon TPDs also coincide with phase changes is unclear due to a lack of experimental data. We did not monitor the ices with the FTIR during warm-up and cannot confirm that there is indeed a crystalline phase transition for any of the experiments.

Thin Ices on Porous H_2O Substrates – All of the hydrocarbons on porous H_2O present both a multilayer and a submonolayer peak, indicating that the targeted ~ 1 ML coverage is achieved. As in the pure ice experiments, 2-carbon hy-

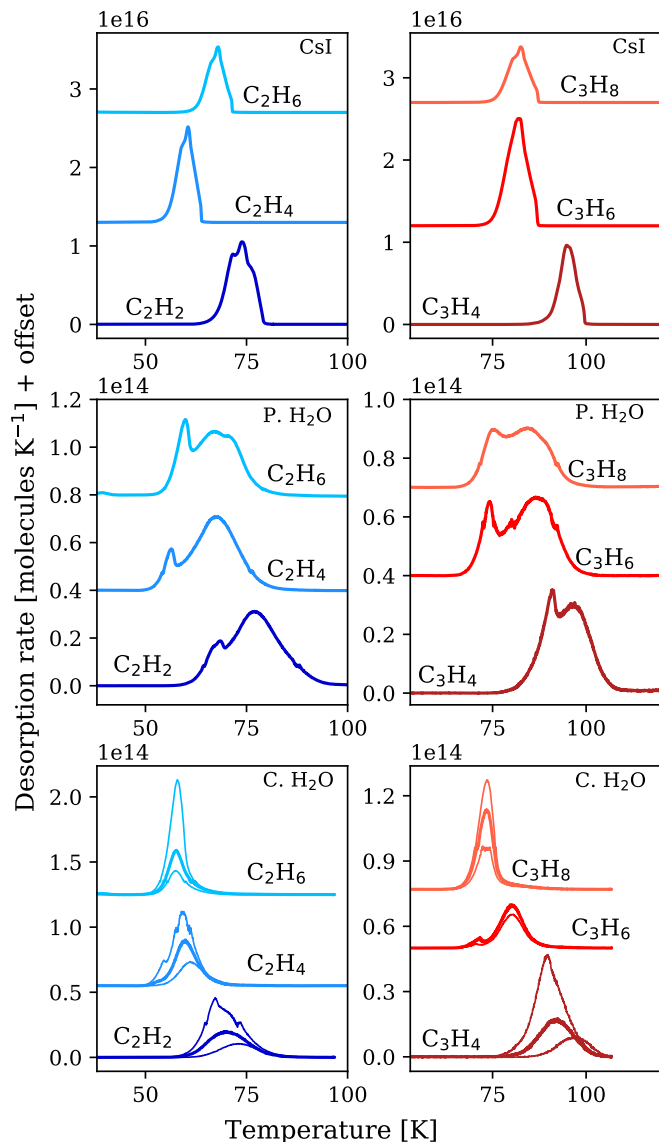


Figure 4. All TPD curves, with TPDs of CsI substrates displayed in the top panels, TPDs of porous H₂O substrates displayed in the middle panels, and TPDs of compact H₂O substrates displayed in the bottom panels. The TPDs on compact H₂O are over-plotted with runs of slightly higher and lower ice coverages for comparison (thinner lines). For all hydrocarbons other than C₂H₆ and C₃H₈, the higher coverage runs feature multilayer peaks that disappear as coverage decreases. The significantly larger desorption rate scale for the pure TPDs compared to the porous and compact TPDs is due to correspondingly larger coverages / amounts of molecules being desorbed. For zeroth-order desorption, the desorption peak shifts to higher temperatures with increasing coverage, which is why the multilayer peaks for the pure and porous TPDs do not perfectly align.

drocarbons have lower desorption temperatures than 3-carbon hydrocarbons. However, the desorption temperature trend changes from that of the pure ice set to alkane, alkene, alkyne for both the 2- and 3-carbon hydrocarbon compact sets. Compared to the compact ice experiments, the porous ice TPD curves appear broader, but as the ice coverages are different no direct comparison is possible. All TPD curves display another large peak near the H₂O desorption temperature (~ 140 – 160 K) due to release of entrapped molecules (not shown here).

Thin Ices on Compact H₂O Substrates – Multiple TPD runs of each hydrocarbon on compact H₂O substrates were taken to explore the effects of ice coverage around the target coverage

of ~ 0.2 ML.

For the alkanes and alkynes, increasing coverage does not produce the double-peaked desorption curve characteristic of a submonolayer that is more strongly bound than subsequent layers. This is in contrast to the alkenes where a lower temperature desorption peak does appear for the thickest coverages, which can be associated with multilayer desorption (Fig. 4). The lack of such a peak for the alkanes and alkynes indicates that the water-hydrocarbon and hydrocarbon-hydrocarbon interactions are of comparable strengths. This is confirmed by the differences in binding energies for pure alkanes and alkynes, which differ from the binding energies of alkanes and alkynes off compact H₂O by only $<10\%$ (see below in Section 3.2). Because we are interested in the hydrocarbon-H₂O interaction, we ran multiple compact TPDs of increasingly thin ices for each molecule until no interaction was visible, then took a slightly higher coverage as the chosen run to ensure that we had isolated the hydrocarbon-H₂O interaction. We verified that the chosen runs had thicknesses of ~ 0.2 ML with the methods previously described in Section 2.2.

As with the pure and porous ices, the 2-carbon hydrocarbons have lower desorption temperatures when compared to the 3-carbon hydrocarbons. As for the porous ice experiments, both the porous 2- and 3-carbon hydrocarbon sets follow the desorption trend of alkane, alkene, alkyne.

3.2. Binding Energies

TPD curves and the resulting binding energy distributions for the 2- and 3-carbon hydrocarbons on H₂O substrates are shown in Fig.’s 2, 5, and 6. Derived binding energies and pre-exponential factors are listed in Table 2. We obtain a range in binding energies of 2200–2800 K for pure 2-carbon hydrocarbon ices and a range of 3500–4200 K for pure 3-carbon hydrocarbon ices. Pre-exponential factors that resulted from fitting the pure ice TPD curves range from $\sim 4 \times 10^{15}$ – 1×10^{19} s⁻¹ and were used to fit the corresponding TPD curves of hydrocarbons on porous and compact H₂O. While these pre-exponential factors are large, they are not unreasonable given that the hydrocarbons in our set are large; higher pre-exponential factors are correlated with larger molecular sizes because larger chain lengths result in higher rotational entropy, which contributes to the pre-exponential factor calculation (Tait et al. 2005). In addition, Smith et al. (2016) report some multilayer C₂H₆ and C₃H₈ pre-exponential factors in the range 10^{16} – 10^{18} s⁻¹, which is consistent with our results, though also report other pre-exponential factors up to ~ 3 x lower for thinner coverages. Ultimately, our derived pre-exponential factors may be too large, but we must adhere to them because they are derived in conjunction with the binding energies, and we emphasize that they are the proper pre-exponential factors that should be used in chemical models. The uncertainties on the pre-exponential factors are from the 2 K absolute error on the temperature instrument (Table 2).

The alkyne and alkene binding energies from desorption off compact H₂O substrates are ~ 5 – 10% higher than the pure hydrocarbon binding energies. The compact alkane binding energies are consistent with the pure binding energies. Lower binding energies for compact ices than pure ices have been observed in the literature for some species, such as atomic oxygen and O₂ (He et al. 2015; Noble et al. 2012). To check that picking coverages of specifically ~ 0.2 ML on compact ices did not result in biased binding energy distributions, we derived distributions for additional experiments of ~ 0.1 – 0.4

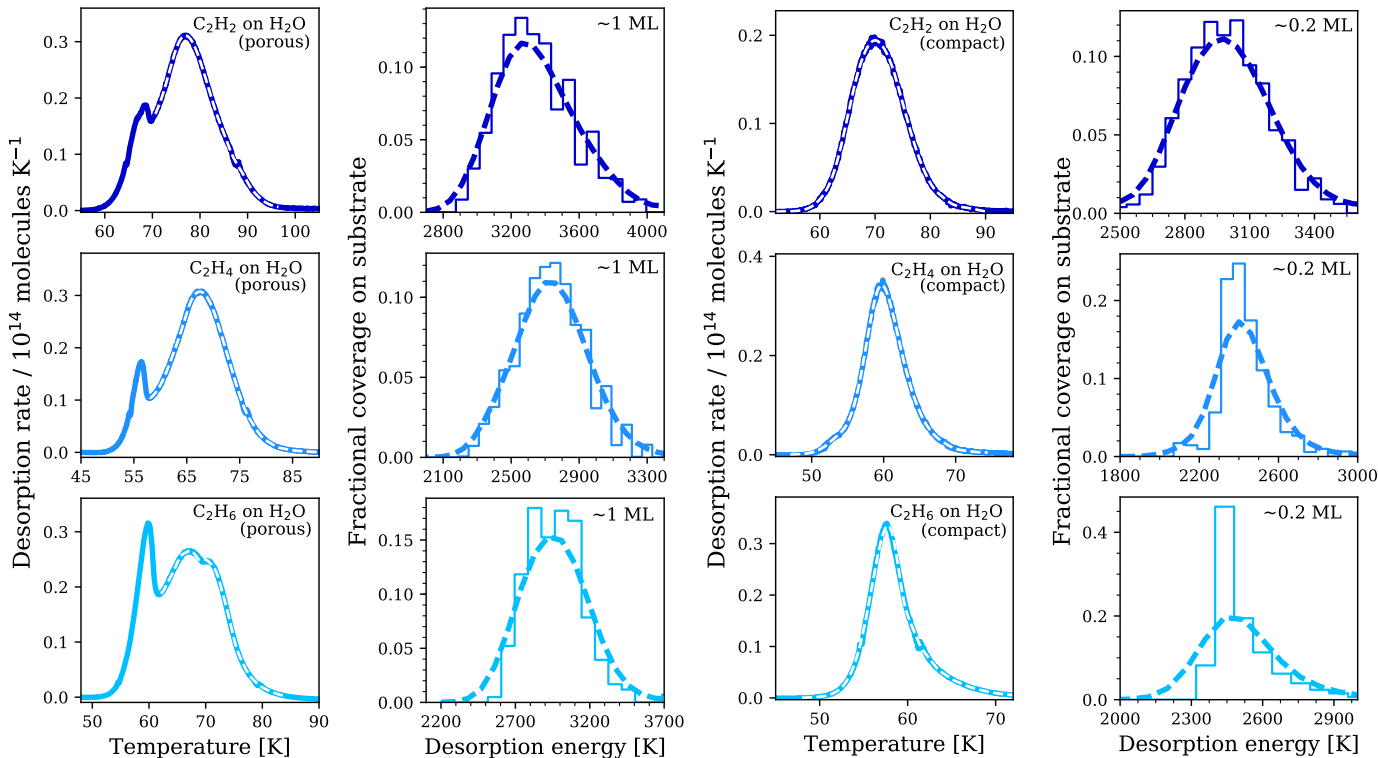


Figure 5. 2-carbon hydrocarbon TPD curves on porous (left) and compact (right) H_2O substrates and corresponding binding energy distributions. TPD curves are displayed in solid colored lines while the white dashed lines represent the fit. The binding energy distributions associated with fractional coverages are shown as the histograms, while the dashed lines represent the smoothed distributions using a Gaussian filter for clarity.

ice coverages on compact ices, and found good agreement between centroids for all coverages (binding energy variation is ~ 200 K at most) (Table 2). For the binding energy distributions, see Fig. A.3. Thus, we conclude that varying ice thicknesses does not affect binding energies significantly if the difference is below a monolayer.

Binding energy values increase when moving from compact to porous H_2O substrate experiments; the binding energies for hydrocarbons desorbing off porous H_2O are ~ 5 – 20% higher (300–500 K) than those of hydrocarbons desorbing off compact H_2O . This is expected as diffusion of adsorbate species into substrate pores leads to availability of higher energy binding sites (e.g., Hornekær et al. 2005; Zubkov et al. 2007; Karssemeijer et al. 2014). This shift should be considered a lower limit because binding energies for ices on H_2O substrates decrease with coverage (Noble et al. 2012), and the porous experiments have substantially higher ice coverages than the compact experiments.

The only binding energies that exist for this set of hydrocarbons in the literature are reported in Smith et al. (2016) for C_2H_6 and C_3H_8 on compact H_2O . Smith et al. (2016) report binding energies of 2500 K and 3200 K for C_2H_6 and C_3H_8 on compact H_2O ice, respectively, which agree well with the binding energies we obtain from our experiments (Table 2). However, more data exist on sublimation enthalpies which can be used to calculate binding energies. A compendium of sublimation enthalpies is reported in (Acree & Chickos 2016) for a large set of compounds that includes all hydrocarbons used in this study except C_3H_4 . When these are converted to binding energies, they also agree well with those obtained from our experiments.

The uncertainties on binding energy values are from the errors in ice thickness and the 2 K absolute error on the temper-

ature instrument. The 2 K error is only relevant in the case of pure binding energy values as the FWHM values of the binding energy distributions for the monolayer and submonolayer experiments are always greater than the uncertainties from the 2 K error (Table 2). We verified that the ice thickness errors have little effect on the binding energies for the pure ices by taking thickness errors of up to 50% and noting only negligible shifts in resultant binding energies and derived pre-exponential values.

4. DISCUSSION

We present the binding energies for C_2H_2 , C_2H_4 , C_2H_6 , C_3H_4 , C_3H_6 , and C_3H_8 from both pure and off porous and compact H_2O substrates. We observe a clear increase in the binding energies between the 2- and 3-carbon hydrocarbons, and the binding energies for the 2-carbon hydrocarbons are higher than the CH_4 binding energies in similar ice environments, presenting a clear trend (Smith et al. 2016; He et al. 2016).

Within the 2- and 3-carbon families and across all ices, the alkanes and alkenes have similar binding energies while the alkyne binding energies are noticeably higher. This is at odds with the assumption that desorption temperatures / binding energies scale with molecular weight, which is sometimes used in astrochemical simulations when experimental data is lacking (Garrod et al. 2008).

For the set of hydrocarbons analyzed, the compact H_2O -hydrocarbon interactions are only slightly stronger (~ 5 – 10%) than the hydrocarbon-hydrocarbon interactions. These results differ from those of studies that constrained the effects of compact H_2O on the binding energies of other molecules, such as CO and N_2 ; Fayolle et al. (2016) determined that the binding energies of CO and N_2 interactions with compact

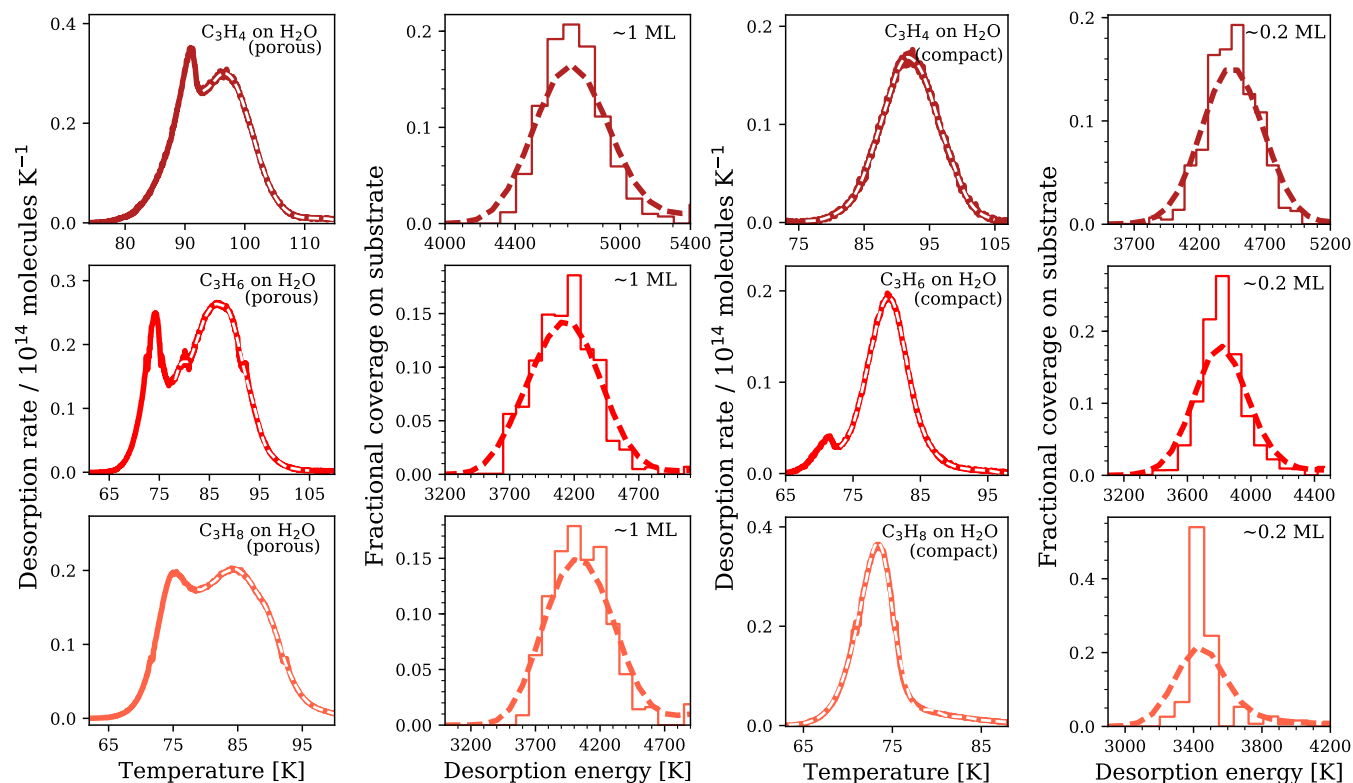


Figure 6. 3-carbon hydrocarbon TPD curves on porous (left) and compact (right) H_2O substrates and corresponding binding energy distributions, similar to Fig. 5

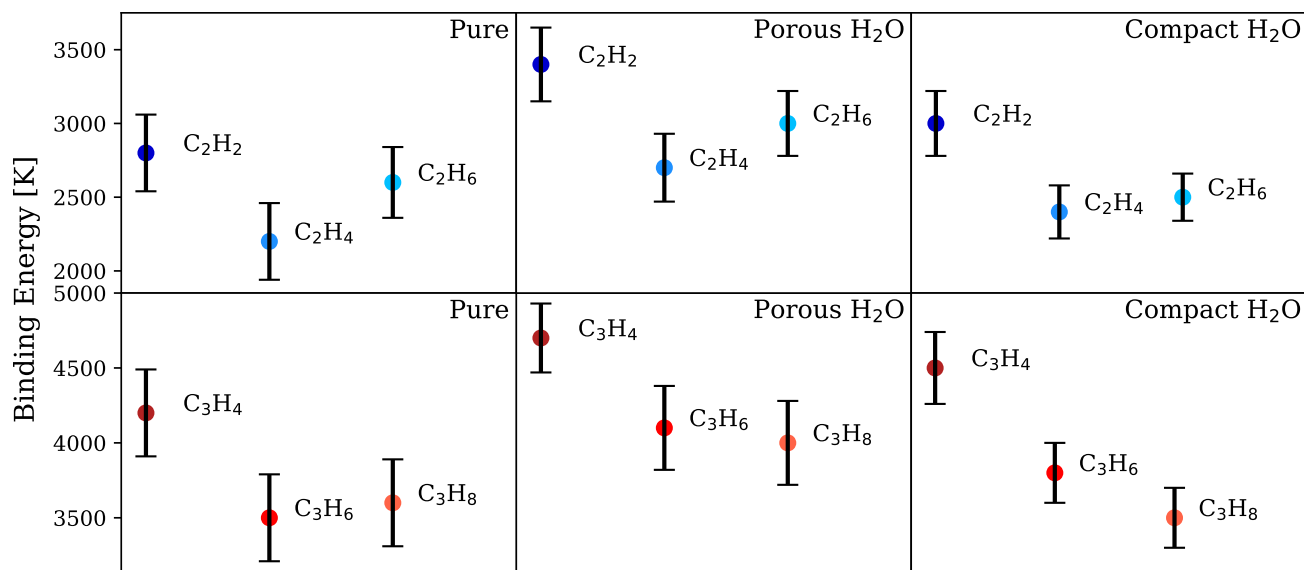


Figure 7. Binding energy values of all TPD experiments. Pure ice binding energy are displayed in the left panels, porous H_2O substrate binding energies are displayed in the middle panels, and compact H_2O substrate binding energies are displayed in the right panels.

H_2O substrates were 30–50% larger than the binding energies of CO and N_2 in pure ices when considering similar ice coverages.

The largest binding energies are achieved on porous H_2O substrates, which is consistent with previous studies of CO and N_2 ices on H_2O (Fayolle et al. 2016; He et al. 2016). However, the increase in binding energies (~ 10 – 20%) from hydrocarbon-hydrocarbon interactions to porous H_2O -hydrocarbon interactions is again relatively low compared to

the $\sim 80\%$ increase of CO and N_2 on porous H_2O (Fayolle et al. 2016). The relatively low shifts in binding energies for the hydrocarbons on H_2O can be explained by their hydrophobic nature, which allows attachment to the H_2O substrate via only weak interactions.

Binding variations for alkanes, alkenes, and alkynes with H_2O may arise from differences in hydrocarbon molecular geometry (size, linearity) due to different bonding structures (single, double, or triple bonds) that create different charge

Table 2
Experimental Summary: Binding Energies for Pure Ice Multilayer Regime TPDs and Mean Binding Energies with FWHMs for Monolayer and Submonolayer Regime TPDs on H₂O Substrates (FWHMs indicated in brackets)

Species	Substrate	Ice Thickness (ML)	T_{des} (K)	ν (s ⁻¹)	E_b (K)
C ₂ H ₂	CsI Window	77 ± 15 ^(a)	74	3 ⁺¹⁷ _{-2.5} × 10 ¹⁶	2800 ⁺²⁰⁰ ₋₃₀₀
C ₂ H ₄	CsI Window	59 ± 12 ^(a)	61	4 ⁺³⁶ _{-3.5} × 10 ¹⁵	2200 ⁺²⁰⁰ ₋₁₀₀
C ₂ H ₆	CsI Window	43 ± 8.6 ^(a)	68	6 ⁺⁴⁴ _{-5.2} × 10 ¹⁶	2600 ⁺³⁰⁰ ₋₂₀₀
C ₃ H ₄	CsI Window	~ 50 ^(b)	95	1 ⁺⁴ _{-0.8} × 10 ¹⁹	4200 ⁺³⁰⁰ ₋₂₀₀
C ₃ H ₆	CsI Window	~ 90 ^(b)	82	6 ⁺³⁴ _{-5.1} × 10 ¹⁸	3500 ⁺³⁰⁰ ₋₃₀₀
C ₃ H ₈	CsI Window	~ 40 ^(b)	83	4 ⁺²⁶ _{-3.4} × 10 ¹⁸	3600 ⁺²⁰⁰ ₋₃₀₀
C ₂ H ₂	Compact H ₂ O	~0.2 (0.1, 0.4) ^(b)	70	3 ⁺¹⁷ _{-2.5} × 10 ¹⁶ (d)	3000 ⁺⁵ ₋₅ [220] (3100, 3010)
C ₂ H ₄	Compact H ₂ O	~0.2 (0.1, 0.4) ^(b)	60	4 ⁺³⁶ _{-3.5} × 10 ¹⁵ (d)	2400 ⁺⁵ ₋₅ [160] (2460, 2360)
C ₂ H ₆	Compact H ₂ O	~0.2 (0.1, 0.4) ^(b)	58	6 ⁺⁴⁴ _{-5.2} × 10 ¹⁶ (d)	2500 ⁺¹⁰ ₋₁₀ [180] (2520, 2480)
C ₃ H ₄	Compact H ₂ O	~0.2 (0.1, 0.4) ^(b)	92	1 ⁺⁴ _{-0.8} × 10 ¹⁹ (d)	4400 ⁺⁵ ₋₅ [240] (4600, 4330)
C ₃ H ₆	Compact H ₂ O	~0.2 (0.1, 0.4) ^(b)	80	6 ⁺³⁴ _{-5.1} × 10 ¹⁸ (d)	3800 ⁺²⁰ ₋₂₅ [200] (3810, 3740)
C ₃ H ₈	Compact H ₂ O	~0.2 (0.1, 0.4) ^(b)	73	4 ⁺²⁶ _{-3.4} × 10 ¹⁸ (d)	3500 ⁺⁵ ₋₅ [200] (3520, 3490)
C ₂ H ₂	Porous H ₂ O	~1 ^(c)	77	3 ⁺¹⁷ _{-2.5} × 10 ¹⁶ (d)	3400 ⁺⁵⁰ ₋₃₀ [250]
C ₂ H ₄	Porous H ₂ O	~1 ^(c)	68	4 ⁺³⁶ _{-3.5} × 10 ¹⁵ (d)	2800 ⁺⁵ ₋₅ [150]
C ₂ H ₆	Porous H ₂ O	~ 1 ^(c)	67	6 ⁺⁴⁴ _{-5.2} × 10 ¹⁶ (d)	3000 ⁺⁴⁰ ₋₂₀ [200]
C ₃ H ₄	Porous H ₂ O	~ 1 ^(c)	97	1 ⁺⁴ _{-0.8} × 10 ¹⁹ (d)	4700 ⁺⁷⁰ ₋₈₀ [230]
C ₃ H ₆	Porous H ₂ O	~ 1 ^(c)	86	6 ⁺³⁴ _{-5.1} × 10 ¹⁸ (d)	4100 ⁺⁵⁰ ₋₆₀ [270]
C ₃ H ₈	Porous H ₂ O	~ 1 ^(c)	84	4 ⁺²⁶ _{-3.4} × 10 ¹⁸ (d)	4000 ⁺⁶⁰ ₋₈₀ [280]

^(a) Derived from IR band strengths, error is taken as 20%.

^(b) Derived from integrated ion currents, error is taken as 50%. Additional binding energies for different submonolayer coverages (~0.1, 0.4) are provided in the E_b column in parentheses.

^(c) Assumed from TPD shape, error is taken as 50%.

^(d) Pre-exponential factors for ices on H₂O are derived from fitting the corresponding pure ice TPDs.

densities and orbital hybridizations. Such steric and electronic effects may impact how the hydrocarbons interact with H₂O. The 2- and 3-carbon family desorption temperature trend of the alkynes exhibiting higher desorption temperatures than the alkenes and alkynes (see Fig. 7) is not obvious, and will require theoretical studies to elucidate.

5. ASTROPHYSICAL IMPLICATIONS

We use our newly-derived binding energies to estimate the sublimation front locations of all six hydrocarbons in a representative protoplanetary disk, characterized by a disk temperature profile $T = 200 \text{ K} \times (r/1 \text{ AU})^{-0.62}$. This is the median disk temperature profile derived from a sample of 24 circumstellar disks in the Taurus-Auriga and Ophiuchus-Scorpius star forming regions (Andrews & Williams 2007).

Because sublimation front locations are set by sublimation temperatures, we use the prescription from Hollenbach et al. (2009) to calculate sublimation temperatures from our binding energies, which is derived by equating the flux of adsorbing and desorbing molecules off a grain surface:

$$T_i \simeq (E_i/k) \left[\ln \left(\frac{4N_i f_i \nu_i}{n_i v_i} \right) \right]^{-1} \quad (3)$$

where T_i is the sublimation temperature, E_i is the binding energy of species i , N_i is the number of adsorption sites per cm² ($N_i \sim 10^{15}$ sites cm²), f_i is the fraction of the surface adsorption sites that are occupied by species i , n_i is the gas-phase

number density of species i , v_i is its thermal speed, and ν_i is the vibrational frequency for which we use our derived pre-exponential factors.

To estimate f_i , we rely on cometary abundances with respect to H₂O because there are no hydrocarbon abundances for protoplanetary disks available. The observed abundances of C₂H₂ and C₂H₆ in cometary ices are 0.2–0.6% with respect to H₂O (Mumma & Charnley 2011). We further adopt abundances of 0.1% for C₂H₄, and 0.01% for the 3-carbon hydrocarbons with respect to H₂O, assuming that cometary abundances decrease by an order of magnitude from CH₄ (1% with respect to H₂O) to C₂H_X, and from C₂H_X to C₃H_X. As cometary ice is ~80% H₂O in composition (Delsemme 1988), we calculate f_i for each hydrocarbon by multiplying the cometary hydrocarbon abundance with respect to water by 0.8 to obtain an estimate of the hydrocarbon surface coverage fraction in icy grain mantles.

We estimate the gas-phase number density n_i by multiplying the number density of atomic hydrogen in protoplanetary disks (which can be regarded as overall density), the H₂O abundance with respect to hydrogen, and the cometary hydrocarbon abundance with respect to H₂O. We take the number density of hydrogen in disks to be 10¹⁰ cm⁻³ in the midplane (e.g., Öberg et al. 2011), and the H₂O abundance to be 10⁻⁴ per H-atom (e.g., Boogert et al. 2015).

We then use the disk temperature profile to estimate sublimation front locations from the sublimation temperatures. We find that the 2-carbon hydrocarbons desorb between 6 and 11

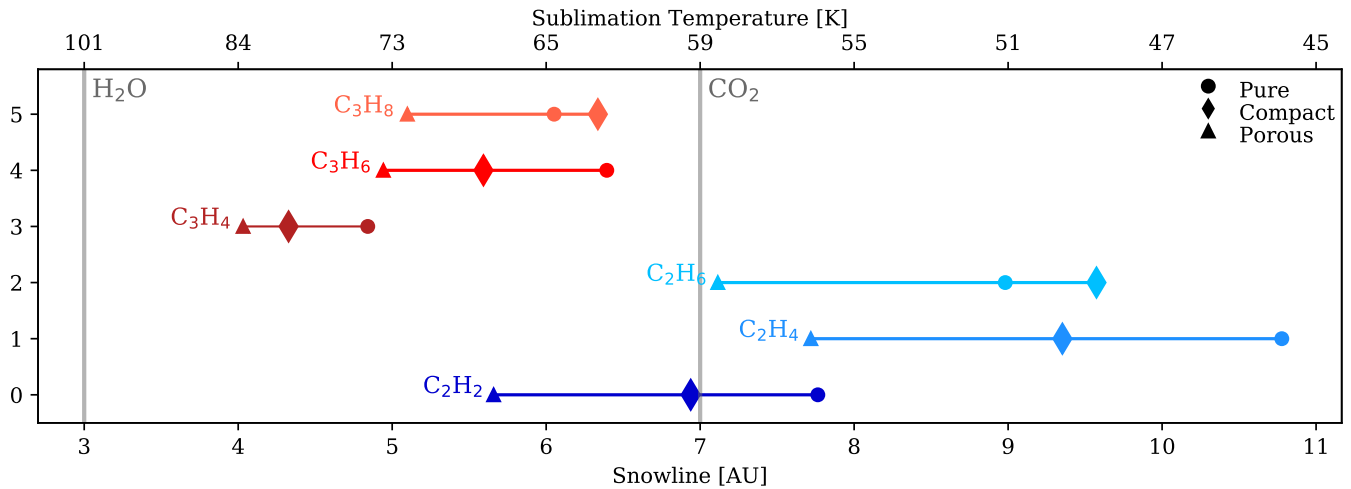


Figure 8. Sublimation front locations calculated from binding energies for each hydrocarbon. Binding energies (porous, compact, and pure) are provided above each sublimation front illustration. Sublimation fronts for H₂O (pure ice) and CO₂ (in non-porous amorphous H₂O-dominated ice) are provided for reference. The H₂O and CO₂ binding energies used for the sublimation front calculations are taken from Fraser et al. (2001) and Noble et al. (2012), respectively.

AU, or ~ 70 K and ~ 50 K, while the 3-carbon hydrocarbons desorb between 4 and 6 AU, or ~ 80 K and ~ 70 K. If we limit ourselves to the most likely case of desorption from grains with compact H₂O mantles, these ranges shrink to 6 and 8 AU for 2-carbon hydrocarbons, and 4 and 6 AU for 3-carbon hydrocarbons (see Fig. 8).

Assuming negligible hydrocarbon entrapment in H₂O ice, any solid bodies that form within 4 AU will be depleted in small hydrocarbons. This potentially limits their ability to participate in ice chemistry and the organic chemistry of planets that they contribute to. In contrast, planetesimals and planets that form outside 8 AU will be rich in hydrocarbons. This includes comets, which can migrate and deliver material to other bodies throughout the disk. However, entrapment is certainly possible, and future studies on entrapment efficiencies of different hydrocarbons are needed to obtain a complete picture of the distributions of small hydrocarbons during planet formation.

6. CONCLUSIONS

In this study, we obtained binding energies C₂H₂, C₂H₄, C₂H₆, C₃H₄, C₃H₆, and C₃H₈ in both pure ices and off porous and compact H₂O. We found:

1. The binding energies of pure 2- and 3-carbon amorphous ices range from 2200–2800 K and 3500–4200 K, respectively.
2. In the submonolayer regime, the binding energies of 2- and 3-carbon amorphous ices off compact H₂O substrates range from 2400–3000 K and 3500–4400 K, respectively. Off porous H₂O substrates, the binding energies of 2- and 3-carbon amorphous ices range from 2800–3400 K and 4000–4700 K, respectively. These porous binding energies are ~ 10 – 20% larger than the pure ice binding energies.
3. Within the 2- and 3-carbon hydrocarbon sets, the alkynes (i.e., least-saturated) hydrocarbons exhibit the largest binding energies.

From these results, we can draw the following conclusions:

1. There is a relatively small difference in binding energies between pure hydrocarbon ices and hydrocarbon ices desorbing off H₂O compared to what has been measured for other volatile species (CO, N₂). This implies that H₂O has a small influence on the snowline locations of these hydrocarbons in protoplanetary disks.
2. Though the alkynes (C₂H₂ and C₃H₄) are the smallest molecules within the 2- and 3-carbon hydrocarbon sets, they exhibit higher binding energies, demonstrating that molecular size does not necessarily correlate with larger desorption temperatures / binding energies within molecular families.

AB acknowledges funding from the Origins of Life Initiative at Harvard. E.C.F.'s contribution was partly carried out at the Jet Propulsion Laboratory, California Institute of Technology, under a contract with the National Aeronautics and Space Administration. KIÖ acknowledges funding from the Simons Collaboration on the Origins of Life Investigator award #321183.

APPENDIX

A. SUPPLEMENTARY FIGURES

REFERENCES

- Acree, W., & Chickos, J. S. 2016, *J. Phys. Chem. Ref. Data*, 45, No. 3
- Agúndez, M., & Wakelam, V. 2013, *Chemical Reviews*, 113, 8710
- Anderson, A., Andrews, B., & Torrie, B. H. 1985, *Journal of Raman Spectroscopy*, 16, 202
- Andrews, S. M., & Williams, J. P. 2007, *ApJ*, 659, 705
- Bernstein, M. P., Sandford, S. A., & Allamandola, L. J. 2005, *J. Phys. Chem. C.*, 161, 53
- Bertin, M., Romanzin, C., Michaut, X., Jeseck, P., & Fillion, J. H. 2011, *ApJS*, 115, 12920
- Betz, A. L. 1981, *ApJ*, 244, L103
- Boogert, A. C. A., Gerakines, P. A., & Whittet, D. C. B. 2015, *ARA&A*, 53, 541
- Bossa, J.-B., Isokoski, K., de Valois, M. S., & Linnartz, H. 2012, *A&A*, 545, A82
- Bossa, J.-B., Isokoski, K., Paardekooper, D. M., et al. 2014, *A&A*, 561, A136
- Brooke, T. Y., Tokunaga, A. T., Weaver, H. A., et al. 1996, *Nature*, 383, 606
- Charnley, S. B. 2004, *Advances in Space Research*, 33, 23
- Cleeves, L. I., Bergin, E. A., Alexander, C. M. O. D. F., et al. 2016, *ApJ*, 819, 13
- Clements, A. R., Berk, B., Cooke, I. R., & Garrod, R. T. 2018, *Physical Chemistry Chemical Physics (Incorporating Faraday Transactions)*, 20, 5553
- Collings, M. P., Anderson, M. A., Chen, R., et al. 2004, *MNRAS*, 354, 1133
- Collings, M. P., Frankland, V. L., Lasne, J., et al. 2015, *MNRAS*, 449, 1826
- Delsemme, A. H. 1988, *Philosophical Transactions of the Royal Society of London Series A*, 325, 509
- Devlin, J. P., & Buch, V. 1995, *The Journal of Physical Chemistry*, 99, 16534
- Doronin, M., Bertin, M., Michaut, X., Phillipe, L., & Fillion, J. H. 2015, *JChPh*, L51
- Fayolle, E. C., Balfe, J., Loomis, R., et al. 2016, *ApJ*, 816, L28
- Fraser, H. J., Collings, M. P., McCoustra, M. R. S., & Williams, D. A. 2001, *MNRAS*, 327, 1165
- Garrod, R. T., Widicus Weaver, S. L., & Herbst, E. 2008, *ApJ*, 682, 283
- Gerakines, P. A., Schutte, W. A., Greenberg, J. M., & van Dishoeck, E. F. 1995, *A&A*, 296, 810
- Gibb, E. L., & Horne, D. 2013, *ApJ*, 776, L28
- Gibb, E. L., Van Brunt, K. A., Brittain, S. D., & Rettig, T. W. 2007, *ApJ*, 660, 1572
- Graninger, D. M., Wilkins, O. H., & Öberg, K. I. 2016, *ApJ*, 819, 140
- Guzmán, V. V., Pety, J., Goicoechea, J. R., et al. 2015, *ApJ*, 800, L33
- Hagen, W., Tielens, A. G. G. M., & Greenberg, J. M. 1981, *Chemical Physics*, 56, 367
- Hardegee-Ullman, E. E., Gudipati, M. S., Boogert, A. C. A., et al. 2014, *ApJ*, 784, 172
- He, J., Acharyya, K., & Vidali, G. 2016, *ArXiv e-prints*, arXiv:1603.02191
- He, J., Emtiaz, S. M., & Vidali, G. 2017, *ApJ*, 851, 104
- He, J., Shi, J., Hopkins, T., Vidali, G., & Kaufman, M. J. 2015, *ApJ*, 801, 120
- Hollenbach, D., Kaufman, M. J., Bergin, E. A., & Melnick, G. J. 2009, *ApJ*, 690, 1497
- Hornekaer, L., Baurichter, A., Petrunin, V. V., et al. 2005, *J. Chem. Phys.*, 122, 124701
- Hudson, R. L., Ferrante, R. F., & Moore, M. H. 2014a, *Icarus*, 228, 276
- Hudson, R. L., Gerakines, P. A., & Moore, M. H. 2014b, *Icarus*, 243, 148
- Hudson, R. L., & Moore, M. H. 1997, *Icarus*, 126, 233
- Isokoski, K., Bossa, J.-B., Triemstra, T., & Linnartz, H. 2014, *Physical Chemistry Chemical Physics (Incorporating Faraday Transactions)*, 16, 3456
- Kaiser, R. I., & Roessler, K. 1998, *ApJ*, 503, 959
- Karssemeijer, L. J., Ioppolo, S., van Hemert, M. C., et al. 2014, *ApJ*, 781, 16
- Kastner, J. H., Qi, C., Gorti, U., et al. 2015, *ApJ*, 806, 75
- Kawakita, H., Dello Russo, N., Vervack, Jr., R., et al. 2014, *ApJ*, 788, 110
- Khanna, R. K., Ospina, M. J., & Zhao, G. 1988, *Icarus*, 73, 527
- Lahuis, F., van Dishoeck, E. F., Boogert, A. C. A., et al. 2006, *ApJ*, 636, L145
- Lauck, T., Karssemeijer, L., Shulenberger, K., et al. 2015, *ApJ*, 801, 118
- Markwick, A. J., Ilgner, M., Millar, T. J., & Henning, T. 2002, *A&A*, 385, 632
- Mastrapa, R. M., Sandford, S. A., Roush, T. L., Cruikshank, D. P., & Dalle Ore, C. M. 2009, *ApJ*, 701, 1347
- Moore, M. H., & Hudson, R. L. 1998, *Icarus*, 135, 518
- Mumma, M. J., & Charnley, S. B. 2011, *ARA&A*, 49, 471
- Mumma, M. J., Disanti, M. A., dello Russo, N., et al. 1996, *Science*, 272, 1310
- Noble, J. A., Congiu, E., Dulieu, F., & Fraser, H. J. 2012, *MNRAS*, 421, 768
- Oba, Y., Miyauchi, N., Hidaka, H., et al. 2009, *ApJ*, 701, 464
- Öberg, K. I., Boogert, A. C. A., Pontoppidan, K. M., et al. 2008, *ApJ*, 678, 1032
- Öberg, K. I., Murray-Clay, R., & Bergin, E. A. 2011, *ApJ*, 743, L16
- Öberg, K. I., van Dishoeck, E. F., Linnartz, H., & Andersson, S. 2010, *ApJ*, 718, 832
- Pontoppidan, K. M., Salyk, C., Bergin, E. A., et al. 2014, *Protostars and Planets VI*, 363
- Qi, C., Öberg, K. I., Wilner, D. J., & Rosenfeld, K. A. 2013, *ApJ*, 765, L14

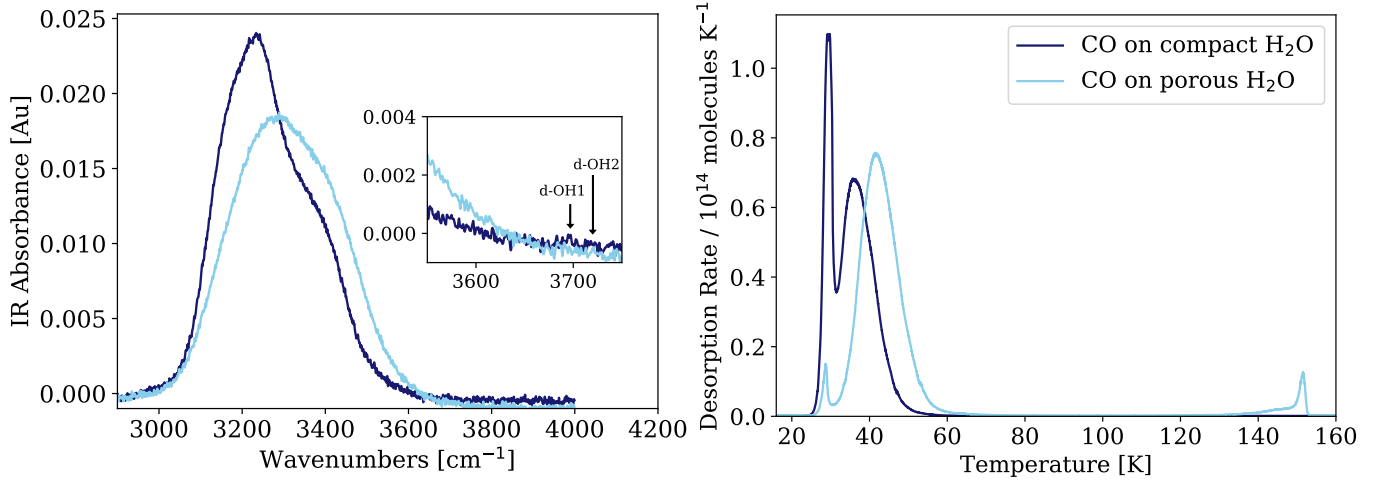


Figure A.1. Left: FTIR data for one representative porous and one compact H₂O ice substrate, with an inset centered on where the dangling O-H bond features would be located (d-O-H1 at ~ 3697 cm⁻¹, d-O-H2 at ~ 3720 cm⁻¹). The degree of porosity cannot be determined from the dangling O-H bond feature as it is not visible in the spectra. Right: TPD curves of CO on compact and porous H₂O substrates. There is a CO desorption peak around the H₂O desorption temperature for the porous substrate experiment, but not for the compact substrate experiment.

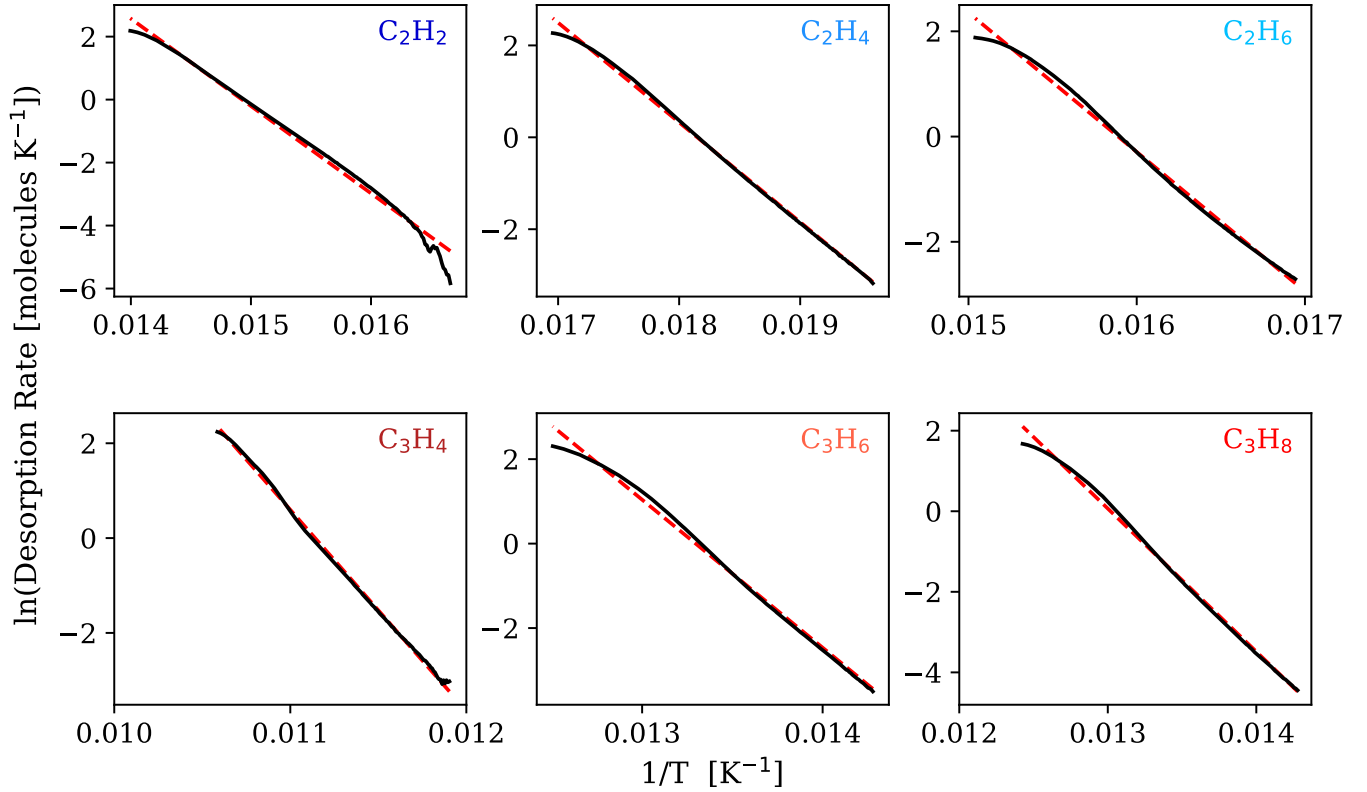


Figure A.2. Arrhenius plots for all pure TPDs with fits to determine the binding energies E_b and pre-exponential factors ν . The desorption rate data are represented by the black lines, while the fits are represented by the dashed red lines.

Raut, U., Famá, M., Teolis, B. D., & Baragiola, R. A. 2007, *J. Chem. Phys.*, 127, 204713
 Sakai, N., & Yamamoto, S. 2013, *Chemical Reviews*, 113, 8981
 Smith, R. S., May, R. A., & Kay, B. D. 2016, *J. Phys. Chem. B*, 120, 1979
 Snyder, L. E., & Buhl, D. 1973, *Nature Physical Science*, 243, 45
 Tait, S. L., Dohnálek, Z., Campbell, C. T., & Kay, B. D. 2005, *J. Chem. Phys.*, 122, 164708
 Thi, W.-F., Ménard, F., Meeus, G., et al. 2011, *A&A*, 530, L2
 Tielens, A. G. G. M., & Hagen, W. 1982, *A&A*, 114, 245

Tucker, K. D., Kutner, M. L., & Thaddeus, P. 1974, *ApJ*, 193, L115
 Viti, S., Collings, M. P., Dever, J. W., McCoustra, M. R. S., & Williams, D. A. 2004, *MNRAS*, 354, 1141
 Zhao, G., Ospina, M. J., & Khanna, R. K. 1988, *Spectrochim. Acta* 44A, 27
 Zubkov, T., Smith, R. S., Engstrom, T. R., & Kay, B. D. 2007, *J. Chem. Phys.*, 127, 184707

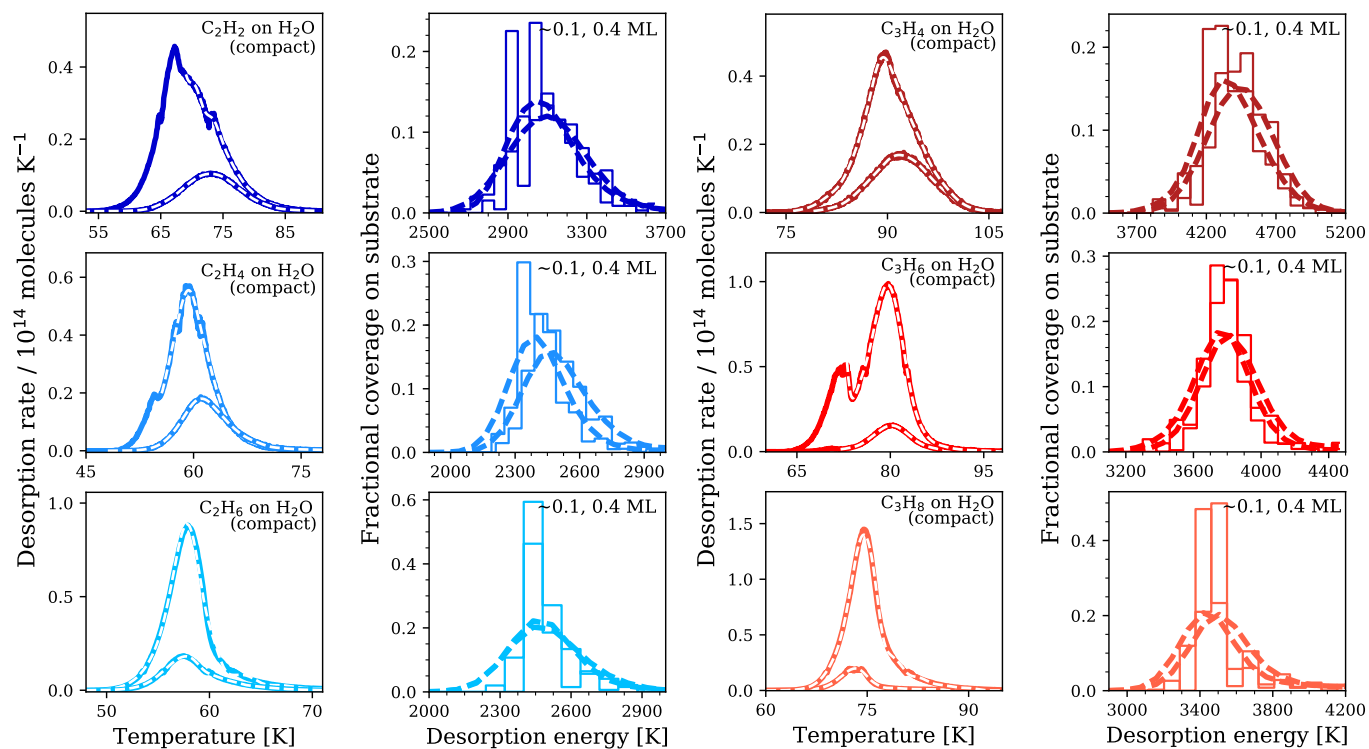


Figure A.3. 2- and 3-carbon hydrocarbon TPD curves on compact H₂O substrates (coverages of ~0.1, 0.4 ML) and corresponding binding energy distributions, similar to Fig.'s 5 and 6. The variation in binding energy distribution centroids for coverages between ~0.1, 0.2 (target coverage), and 0.4 ML is less than 200 K for all hydrocarbons used in this study.